Remodeling of E-cadherin subcellular localization during cell dissemination

Alejandra J. H. Cabrera[a], Barry M. Gumbiner[a,b,c], and Young V. Kwon[a,*]
[a]Department of Biochemistry, University of Washington, Seattle, WA 98195; [b]Center for Developmental Biology and Regenerative Medicine, Seattle Children's Research Institute, Seattle, WA 98101; [c]Department of Pediatrics, University of Washington School of Medicine, Seattle, WA 98195

ABSTRACT **Given the role of E-cadherin (E-cad) in holding epithelial cells together, an inverse relationship between E-cad levels and cell invasion during the epithelial-mesenchymal transition and cancer metastasis has been well recognized. Here we report that E-cad is necessary for the invasiveness of *Ras*^{V12}-transformed intestinal epithelial cells in *Drosophila*. E-cad/β-catenin disassembles at adherens junctions and assembles at invasive protrusions—the actin- and cortactin-rich invadopodium-like protrusions associated with the breach of the extracellular matrix (ECM)—during dissemination of *Ras*^{V12}-transformed intestinal epithelial cells. Loss of E-cad impairs the elongation of invasive protrusions and attenuates the ability of *Ras*^{V12}-transformed cells to compromise the ECM. Notably, E-cad and cortactin affect each other's localization to invasive protrusions. Given the essential roles of cortactin in cell invasion, our observations indicate that E-cad plays a role in the invasiveness of *Ras*^{V12}-transformed intestinal epithelial cells by controlling cortactin localization to invasive protrusions. Thus our study demonstrates that E-cad is a component of invasive protrusions and provides molecular insights into the unconventional role of E-cad in cell dissemination in vivo.**

Monitoring Editor
Elizabeth Chen
University of Texas
Southwestern Medical Center

Received: Mar 10, 2023
Accepted: Mar 22, 2023

INTRODUCTION

E-cadherin (E-cad), the main component of adherens junctions, helps to hold epithelial cells together (Burdsal *et al.*, 1993; Larue *et al.*, 1994; Gumbiner, 2005; Harris and Tepass, 2010; Mendonsa *et al.*, 2018). To invade and migrate, cells disintegrate adherens junctions to free themselves from neighboring cells (Mendonsa *et al.*, 2018; Onder *et al.*, 2008; Vleminckx *et al.*, 1991). When epithelial cells invade and migrate during development, they undergo epithelial-to-mesenchymal transition (EMT), a process that allows them to acquire the properties of mesenchymal cells (Cano *et al.*, 2000; Strobl-Mazzulla and Bronner, 2012). Consistent with the role of E-cad, loss of E-cad is considered to be a hallmark of EMT (Hajra *et al.*, 2002; Thiery *et al.*, 2009). Frixen *et al.* showed that loss of E-cad is also important for the ability of carcinoma cells to invade and migrate in culture (Frixen *et al.*, 1991). These observations coincide with clinical reports indicating that E-cad is frequently reduced in epithelial cell cancers (Berx *et al.*, 1995; Bogenrieder and Herlyn, 2003). Therefore reduction of E-cad is thought to promote cancer cell invasion and metastasis (Frixen *et al.*, 1991; Perl *et al.*, 1998; Semb and Christofori, 1998; Christofori and Semb, 1999; Berx and Van Roy, 2001; Herzig *et al.*, 2007; Petrova *et al.*, 2016; Padmanaban *et al.*, 2019; Na *et al.*, 2020). However, several clinical studies have reported that E-cad is expressed in multiple metastatic tumors (Sundfeldt *et al.*, 1997; Kleer *et al.*, 2001; Di Venosa *et al.*, 2012; Kim *et al.*, 2016). Notably, Padmanaban *et al.* have recently demonstrated that E-cad is required for metastasis in multiple invasive ductal carcinoma models by helping cancer cells to survive after dissemination (Padmanaban *et al.*, 2019), suggesting that E-cad might play a more complex, not fully defined, role in metastasis of cancer cells.

Here we attempted to address the role of E-cad in the invasiveness of transformed cells in their native microenvironment by

This article was published online ahead of print in MBoC in Press (http://www.molbiolcell.org/cgi/doi/10.1091/mbc.E23-03-0087) on March 29, 2023.

Conflict of interest: The authors declare no competing interests.

Author contributions: A.J.H.C., Y.V.K., and G.M.G. designed experiments, analyzed data, and wrote the manuscript; A.J.H.C. performed experiments.

*Address correspondence to: Young V. Kwon (ykwon7@uw.edu).

Abbreviations used: ABD, actin binding domain; Arm, Armadillo; CadN, Cadherin-N; DAPI, 4′6′-diamidino-2-phenylindole; EB, enteroblast; E-cad, E-cadherin; ECM, extracellular matrix; EMT, epithelial-mesenchymal transition; GFP, green florescent protein; ISC, intestinal stem cell; MMP1, Matrix metalloprotease 1; Moe, Moesin; RFP, red florescent protein; RNAi, RNA interference; UAS, upstream activation sequence; VM, visceral muscle.

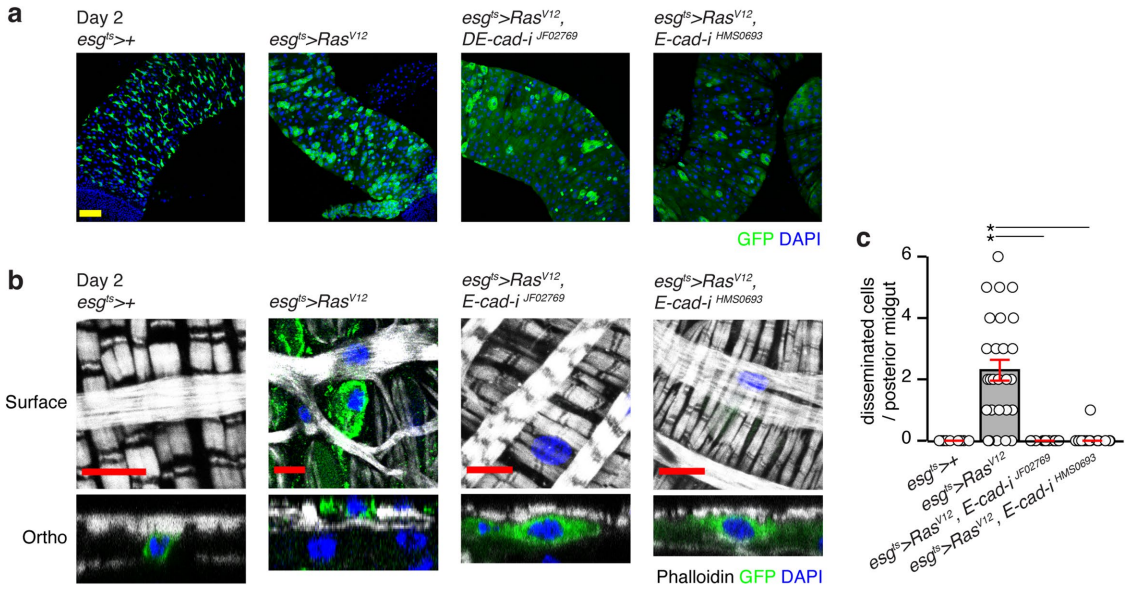

FIGURE 1: E-cad is necessary for cell dissemination. (a) Posterior midguts at day 2 of transgene expression by *esg*^{ts}. Two *E-cad* RNAi lines used to knock down *E-cad* are indicated as *E-cad-i*^{JF02769} or *E-cad-i*^{HMS0693}. Cells manipulated by *esg*^{ts} are labeled with GFP (green), and nuclei are stained with DAPI (blue). Scale bar, 50 μm. (b) Surface views and orthogonal images of representative cells; *esg*^{ts}>+, control cell residing in the intestinal epithelium; *esg*^{ts}>*Ras*^{V12}, representative disseminated *Ras*^{V12} cell residing at the outer surface of the VM; *esg*^{ts}>*Ras*^{V12}, *E-cad-i*^{JF02769} *and esg*^{ts}>*Ras*^{V12}, *E-cad-i*^{JF02769} cell, representative E-cad depleted *Ras*^{V12} cells residing in the intestinal epithelium. The VM is visualized with phalloidin (gray), *Ras*^{V12} cells are marked with GFP (green), and nuclei are stained with DAPI (blue). Scale bar, 10 μm. (c) Quantification of disseminated cells residing on the outer VM surface at the posterior midguts. From left to right, $P = 4.40 \times 10^{-9}$ (*Ras*^{V12} - *Ras*^{V12}, *E-cad-i*^{JF02769}) and $P = 1.10 \times 10^{-9}$ (*Ras*^{V12} - *Ras*^{V12}, *E-cad-i*^{HMS0693}); $n = 12$ (*esg*^{ts}), $n = 27$ (*esg*^{ts}>*Ras*^{V12}), $n = 13$ (*esg*^{ts}>*Ras*^{V12}, *E-cad-i*^{JF02769}), and $n = 16$ (*esg*^{ts}>*Ras*^{V12}, *E-cad-i*^{HMS0693}) midguts. Statistical analysis was performed using one-way ANOVA with post-hoc Tukey HSD. Asterisks indicate statistical significance (*$P < 0.05$).

employing our *Drosophila* model of *Ras*^{V12}-transformed cell dissemination (Lee *et al.*, 2020). Expression of *Ras*^{V12} in adult intestinal stem cells (ISCs) and enteroblasts (EBs), using the conditional GAL4 driver *esg-GAL4*, *UAS-GFP*, *tub-GAL80*^{ts} (*esg*^{ts}; see *Methods*), allows *Ras*^{V12}-expressing intestinal epithelial cells (*Ras*^{V12} cells) to disseminate basally from the midgut and enter the hemocoel—the primary cavity containing circulatory fluid (Kwon *et al.*, 2015; Lee *et al.*, 2020) (Supplemental Figure S1). Note that *Ras*^{V12} cells also delaminate apically toward the lumen and then are presumably excreted (Lee *et al.*, 2020). During dissemination, *Ras*^{V12} cells generate actin- and cortactin-rich invasive protrusions, functionally and structurally reminiscent of invadopodia observed in cancer cells, to breach the ECM and the visceral muscle (VM) layer (Clark *et al.*, 2007; Eddy *et al.*, 2017; Lee *et al.*, 2020; Lohmer *et al.*, 2014; Parekh and Weaver, 2016). After compromising the integrity of the ECM and the VM, *Ras*^{V12} cells can then migrate into the circulation by bleb-driven movement. We have previously discovered that knockdown of *Cortactin* or the mechanosensitive channel *Piezo* specifically in *Ras*^{V12} cells attenuates dissemination of *Ras*^{V12} cells by impairing their ability to invade and migrate across the ECM and the VM (Lee *et al.*, 2020). Thus this model allows us not only to observe the cell dissemination process in a native context at the cellular and molecular levels but also to test the function of genes in the cell dissemination process using the advanced genetic tools available in *Drosophila*.

In this study, we demonstrate that E-cad is necessary for the invasiveness of *Ras*^{V12} cells during cell dissemination in vivo. Subcellular E-cad is redistributed in disseminating *Ras*^{V12} cells: E-cad disassembles at adherens junctions—a process that recapitulates the functional consequence of E-cad loss during EMT—and assembles at invasive protrusions, which is not a conventional location for E-cad. Our observations indicate that E-cad is required for the generation of elongated and functional invasive protrusions in part by controlling the localization of cortactin to the protrusions. Therefore our study provides new insights into the role of E-cad in cell invasion during cell dissemination.

RESULTS

E-cad is required for the dissemination of *Ras*^{V12} cells

Since our knowledge of the role of E-cad in cell dissemination is limited, we initiated our study by testing whether E-cad is necessary for this process. Knockdown of *Drosophila E-cad* (also known as *shotgun* [*shg*]) in *Ras*^{V12} cells by expressing *E-cad* RNA interference (RNAi) (*JF02769* and *HMS00693*) with *esg*^{ts} did not dramatically alter the overall distribution of *Ras*^{V12} cells in the posterior midguts (Figure 1a). At day 2 of *Ras*^{V12} expression, disseminated *Ras*^{V12} cells residing at the outer surface of the posterior midgut can be quantified to assess cell dissemination (Figure 1b and Supplemental Figure S1c) (Lee *et al.*, 2020). However, E-cad depletion in *Ras*^{V12} cells almost eliminated disseminated *Ras*^{V12} cells detected at the outer surface of the posterior midguts (Figure 1, b and c). At day 2 of *Ras*^{V12} expression, *Ras*^{V12} cells also apically delaminate (Supplemental Figure S1, b and c). Interestingly, E-cad depletion did not impair apical delamination of *Ras*^{V12} cells (Supplemental Figure S2), suggesting that the inability to move out from the epithelium was not likely to account for the observed cell dissemination defect to the surface of the midgut. Altogether, we concluded that E-cad was necessary for cell dissemination.

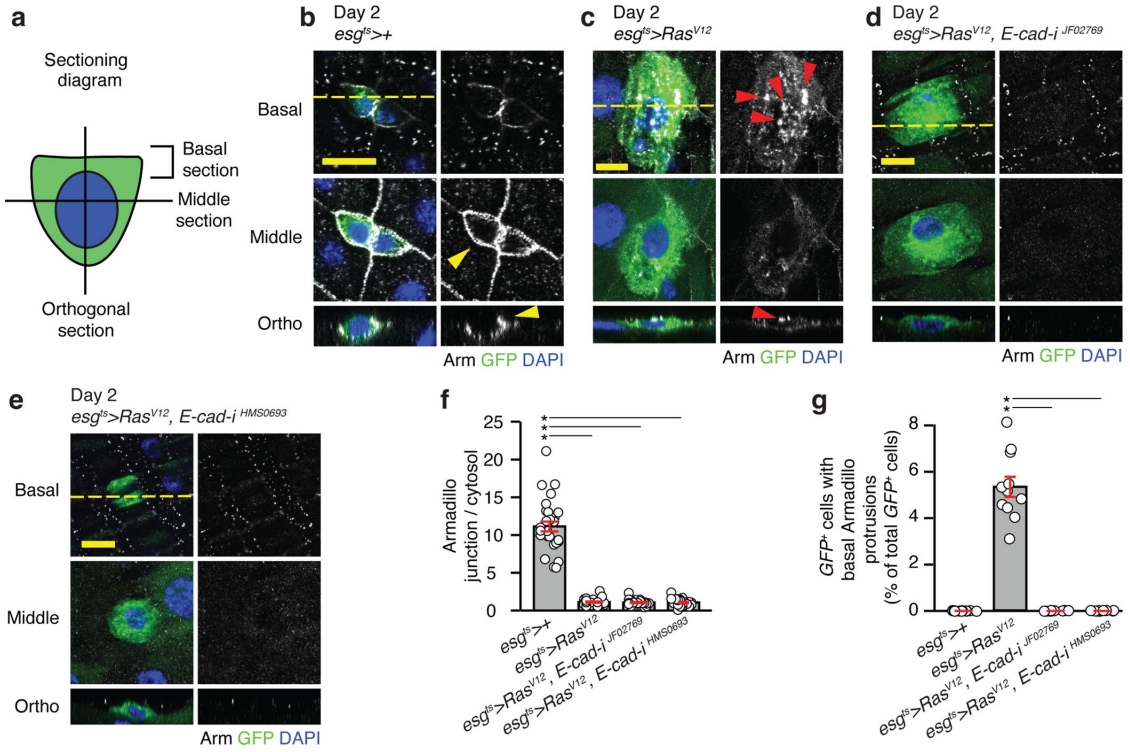

FIGURE 2: E-cad dissembles at cell–cell junction and assembles at the basal side of *Ras^{V12}* cells during dissemination. (a–e) Representative images of cells stained with anti-Arm antibody (gray). Genotypes are shown. Top images representing the basal section of the cells, projections of two to four very basal z-stacks. Middle images show cross-sections capturing cell–cell junction regions of the cells. In the orthogonal views, the basal side of cells is positioned upward. Yellow arrowheads indicate Arm signals detected at cell–cell junctions, and red arrowheads indicate Arm signals detected as distinct puncta at the basal side of *Ras^{V12}* cells. Scale bar, 10 μm. (f) Quantification of Arm signal at cell junctions normalized to cytosolic Arm signal. From left to right, $P = 1.43 \times 10^{-13}$ (*esg^{ts} - Ras^{V12}*), $P = 1.50 \times 10^{-13}$ (*esg^{ts} - Ras^{V12}, E-cad-i^{JF02769}*), $P = 1.44 \times 10^{-13}$ (*esg^{ts} - Ras^{V12}, E-cad-i^{HMS0693}*). $n = 30$ cells from 10 midguts per genotype. (g) Total percentage of cells with Arm basal puncta per gut. From left to right, $P = 1.64 \times 10^{-5}$ (*Ras^{V12} - Ras^{V12}, E-cad-i^{JF02769}*) and $P = 8.94 \times 10^{-6}$ (*Ras^{V12} - Ras^{V12}, E-cad-i^{HMS0693}*); $n = 12$ (*esg^{ts}*), $n = 11$ (*esg^{ts}>Ras^{V12}*), $n = 8$ (*esg^{ts}>Ras^{V12}, E-cad-i^{JF02769}*), and $n = 9$ (*esg^{ts}>Ras^{V12}, E-cad-i^{HMS0693}*) midguts. Mean ± SEM are shown with individual data points. Statistical analysis was performed using one-way ANOVA with post-hoc Tukey HSD. Asterisks indicate statistical significance (*$P < 0.05$).

The subcellular distribution of E-cad/Arm is remodeled during in vivo cell dissemination

We next scrutinized the subcellular distribution of E-cad in *Ras^{V12}* cells to gain insight into how adherens junctions were affected during cell dissemination. At day 1 of *Ras^{V12}* expression, most of the *Ras^{V12}* cells stay in the midgut epithelium, resulting in hyperplasia (Lee *et al.*, 2020). At day 2, *Ras^{V12}* cells basally disseminate from the midgut while a significant number of *Ras^{V12}* cells also delaminate apically toward the lumen (Lee *et al.*, 2020) (Supplemental Figures S1 and S2). When we stained control and *Ras^{V12}* cells at day 1 with anti-E-cad antibody, strong signals were detected at the lateral side (Supplemental Figure S3a), which was recapitulated by staining for the *Drosophila* β-catenin ortholog Armadillo (Arm) (Supplemental Figure S3b). Since Arm staining yielded much less background signal at the VM (Supplemental Figure S3, a and b, nonspecific signals in the VM layer are indicated with asterisks), we decided to use Arm staining as the primary method to assess E-cad subcellular distribution. At day 2 of *Ras^{V12}* expression, Arm signals were no longer clearly visible at the lateral side of *Ras^{V12}* cells (Figure 2, a–e, middle section, and f), suggesting that disassembly of adherens junctions was a mechanism to aid in the dissemination of *Ras^{V12}* cells. Notably, we detected Arm signals as discrete puncta at the basal side of *Ras^{V12}* cells (Figure 2c, basal section, red arrowheads, and g). These basal Arm signals were not visible in control cells (Figure 2, a and g) or *Ras^{V12}* cells at day 1 (Supplemental Figure S3b). E-cad was also detected as puncta at the basal side of *Ras^{V12}* cells when we stained with anti-E-cad antibody or used the E-cad protein-trap line (*shg^{mTomato}*) producing E-cad-mTomato fusion (E-cad^{mTomato}) under the control of its own promotor (Supplemental Figure S3, c and d). Additionally, Arm colocalized with E-cad^{mTomato} at the basal side of *Ras^{V12}* cells (Supplemental Figure S3d), and *E-cad* knockdown impaired the formation of Arm puncta at the basal side of *Ras^{V12}* cells (Figure 2, d, e, and g), indicating that the formation of these puncta was dependent on E-cad. Taken together, these observations demonstrate that E-cad/Arm undergoes extensive remodeling during dissemination of *Ras^{V12}* cells. E-cad disassembles at adherens junction and assembles as puncta at the basal side of *Ras^{V12}* cells.

E-cad/Arm assembles at invasive protrusions

The unconventional E-cad/Arm puncta at the basal side of *Ras^{V12}* cells are reminiscent of *Drosophila* invasive protrusions, which are actin- and cortactin-rich protrusions associated with degradation of the ECM and the VM (Lee *et al.*, 2020). Thus we tested whether E-cad/Arm was localized at invasive protrusions. Considering the possible limitations associated with various actin markers (Belin *et al.*, 2014; Spracklen *et al.*, 2014), we decided to use three different actin reporters, Lifeact-mRFP (Belin *et al.*, 2014; Riedl *et al.*, 2008), mCherry-Moe.ABD (Millard and Martin, 2008), and actin-mRFP

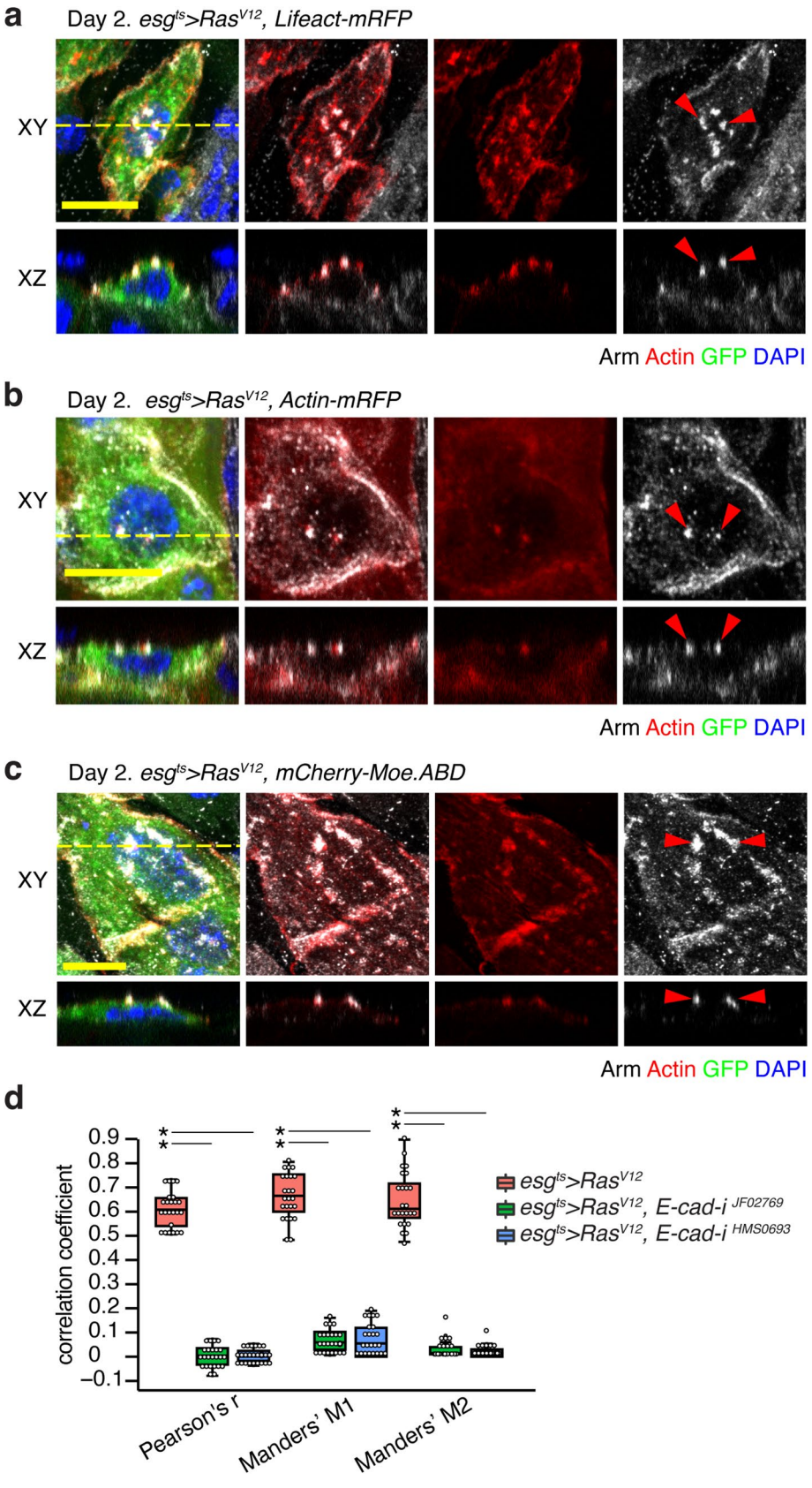

FIGURE 3: E-cad/Arm assembles at invasive protrusions. Basal sections (xy) and orthogonal views (xz) of *Ras*^{V12} cells. Transgenes are induced for 2 d. (a–c) Actin (red) is visualized with *UAS-Lifeact-mRFP* (a), *UAS-Actin-mRFP* (b), and *UAS-mCherry-Moe.ABD* (c). Arm (gray) was detected by staining with anti-Arm antibody. In the orthogonal views, the basal side of cells is positioned upward. Colocalization of an actin marker and Arm is indicated with arrowheads. Nuclei are stained with DAPI (blue). Scale bars, 10 μm. (d) Colocalization analysis for Arm and actin markers at the basal side of *Ras*^{V12} cells. Pearson's r value and Manders' coefficients (M1 and M2) were computed. Results are shown in boxplots (center line, median; box, IQR; whiskers extending to ± 1.5 × IQR). For Pearson's r, $P = 4.98 \times 10^{-9}$ (*Ras*^{V12} - *Ras*^{V12}, *E-cad-i*^{JF02769}) and $P = 1.16 \times 10^{-8}$ (*Ras*^{V12} - *Ras*^{V12}, *E-cad-i*^{HMS0693}). For Manders' M1, $P = 5.62 \times 10^{-9}$ (*Ras*^{V12} - *Ras*^{V12}, *E-cad-i*^{JF02769}) and $P = 9.34 \times 10^{-9}$ (*Ras*^{V12} - *Ras*^{V12}, *E-cad-i*^{HMS0693}). For Manders' M2, $P = 2.68 \times 10^{-8}$ (*Ras*^{V12} - *Ras*^{V12}, *E-cad-i*^{JF02769}) and $P = 1.86 \times 10^{-9}$ (*Ras*^{V12} - *Ras*^{V12}, *E-cad-i*^{HMS0693}); $n = 36$ cells from 16 midguts (*esg*^{ts}>*Ras*^{V12}), $n = 24$ cells from 12 midguts (*esg*^{ts}>*Ras*^{V12}, *E-cad-i*^{JF02769}), and $n = 24$ cells from 12 midguts (*esg*^{ts} > *Ras*^{V12}, *E-cad-i*^{HMS0693}). The statistical significance was assessed by Kruskal–Wallis and Dunn's test. Asterisks indicate statistical significance ($P < 0.05$). If not noted, differences were not significant at the 0.05 level.

(Liu *et al.*, 2008) to visualize invasive protrusions (Figure 3, a–c, arrowheads). Importantly, Arm signals co-localized to the puncta marked by the actin markers (Figure 3, a–c, arrowheads, and d). Cortactin is also enriched in invasive protrusions (Lee *et al.*, 2020). Since cortactin is abundantly expressed in all types of cells including the VM, we cannot stain cortactin to visualize invasive protrusions in *Ras*^{V12} cells. Alternatively, expressing cortactin-HA specifically in *Ras*^{V12} cells using *esg*^{ts} and staining for HA allows us to mark invasive protrusions in *Ras*^{V12} cells (Lee *et al.*, 2020). We found that cortactin-HA and Arm co-localized as puncta at the basal side of *Ras*^{V12} cells (Supplemental Figure S4). Thus these results indicate that E-cad/Arm is a new component of invasive protrusions.

E-cad is required for elongation of invasive protrusions and the ability of *Ras*^{V12} cells to compromise the ECM and VM

Given that Arm signals were found in invasive protrusions, we decided to deplete E-cad in *Ras*^{V12} cells to address whether E-cad plays a role in the assembly and function of invasive protrusions. Expression of *E-cad* RNAi with *esg*^{ts} did not alter the formation of Lifeact-RFP puncta at the basal side of *Ras*^{V12} cells; neither the number of cells with Lifeact-RFP puncta nor the number of Lifeact-RFP puncta per cell were significantly altered after E-cad depletion (Figure 4, a–c). These results suggest that E-cad is not crucial for the formation of invasive protrusions. *E-cad* depletion resulted in an overall loss of

Arm signals in *Ras^{V12}* cells (Figure 2a–e). Thus colocalization between Arm signals and Lifeact-RFP was almost negligible (Figure 4a). Notably, *E-cad* knockdown resulted in a significant decrease in the length of invasive protrusions (Figure 4d). The length of invasive protrusions in *Ras^{V12}* cells showed a multimodal distribution (Figure 4e, pink). Interestingly, the global distribution is positively skewed: we saw a peak at 3.2 µm (Figure 4e, arrowhead), followed by a population even taller than 4 µm (Figure 4e, bracket). When *E-cad* RNAi was expressed in *Ras^{V12}* cells, the length distribution of invasive protrusions became narrower mainly because the longer invasive protrusion population was lost: the peak at 3.2 µm detected in *Ras^{V12}* cells was negligible, and invasive protrusions taller than 4 µm were almost absent (Figure 4e, green and blue). Therefore these results suggest that E-cad plays an important role in the elongation of invasive protrusions.

Next, we assessed whether *E-cad* knockdown impaired the ability of *Ras^{V12}* cells to degrade the ECM and the VM. At day 2 of *Ras^{V12}* expression, the laminin layer was almost completely degraded (Figure 4, f and g). In contrast, the laminin layer remained intact when E-cad was depleted in *Ras^{V12}* cells (Figure 4, f and g). *Drosophila* invasive protrusions have been shown to damage the VM layer—manifested by occasional breakages of the longitudinal muscles that normally span the whole posterior part of the midgut (Lee *et al.*, 2020) (Figure 4, h and i). E-cad depletion in *Ras^{V12}* cells significantly reduced the number of longitudinal muscle breakages (Figure 4, h and i). These results show that E-cad plays an essential role in the invasiveness of *Ras^{V12}* cells by controlling the function of invasive protrusions. Without E-cad, *Ras^{V12}* cells lose their ability to compromise the ECM and the VM for dissemination.

In cancer cells, functional invadopodia, which are elongated and can degrade the ECM, are generated by the formation and maturation processes (Magalhaes *et al.*, 2011; Jeannot and Besson, 2020). Likewise, our previous study suggests that the formation of invasive protrusions, which are characterized by the appearance of actin-rich puncta at the basal side of *Ras^{V12}* cells, can be separated from the generation of functional invasive protrusions (Lee *et al.*, 2020). Here we show that invasive protrusions are heterogenous in size (Figure 4e). Furthermore, our findings demonstrate that the elongated and relatively shorter invasive protrusions are genetically separable (Figure 4e). Thus we propose that the generation of elongated and functional invasive protrusions might require a process that resembles invadopodium maturation.

E-cad and cortactin influence each other's localization at invasive protrusions

Cortactin is a key regulator of invadopodium formation, maturation, and disassembly (Jeannot and Besson, 2020). Our previous study showed that cortactin is also required for the function of invasive protrusions, suggesting that cortactin might play a similar role in the assembly and function of invasive protrusions (Lee *et al.*, 2020). Depletion of cortactin impaired the ability of *Ras^{V12}* cells to degrade the ECM and the VM (Lee *et al.*, 2020), reminiscent of the phenotypes caused by E-cad depletion. Considering the phenotypic similarity, E-cad and cortactin might interact to control invasive protrusions. Interestingly, it has been shown that cortactin and E-cad require each other for proper localization at the cell–cell contacts in MCF7 monolayers (Helwani *et al.*, 2004; Ren *et al.*, 2009). Thus we decided to test whether E-cad is required for the localization of cortactin at invasive protrusions, and vice versa.

To determine the role of E-cad in the localization of cortactin to invasive protrusions, we tested whether E-cad depletion impaired the formation of cortactin-rich puncta at the basal side of *Ras^{V12}* cells. To assess the subcellular distribution of cortactin, we expressed *UAS-Cortactin-HA* specifically in *Ras^{V12}* cells (Lee *et al.*, 2020). When E-cad was depleted, *Ras^{V12}*cells showing cortactin-rich puncta were significantly reduced (Figure 5a). In most of the E-cad-depleted *Ras^{V12}* cells, cortactin-HA signals appeared to be enriched at the basal side; however, discrete cortactin-rich puncta were rarely detected at the basal side (Figure 5b). Next, we tested whether cortactin affects E-cad/Arm localization to invasive protrusions. Expression of *Cortactin RNAi* significantly reduced the proportion of *Ras^{V12}* cells with Arm puncta at the basal side, and in most of the cortactin-depleted *Ras^{V12}* cells, Arm-rich puncta were not detectable at the basal side (Figure 5, c and d). Together, these results suggest that cortactin and E-cad influence each other's localization at invasive protrusions.

Cortactin plays a key role in both formation and elongation of invasive protrusions

Cortactin-mediated formation of a branched actin network plays an important role during invadopodium maturation (Uruno *et al.*, 2001; Weaver *et al.*, 2001; Clark *et al.*, 2007). If cortactin plays similar roles in the elongation of invasive protrusions, the phenotypes caused by E-cad depletion might be explained by the inability to recruit cortactin to invasive protrusions. Thus we measured invasive protrusion length using Lifeact after depleting cortactin in *Ras^{V12}* cells. We noticed that cortactin depletion significantly reduced the proportion of *Ras^{V12}* cells showing Lifeact puncta at the basal side (Figure 6, a and b), suggesting a role for cortactin in the formation of invasive protrusions. Note that E-cad depletion reduced neither the proportion of *Ras^{V12}* cells showing Lifeact puncta nor the number of invasive protrusions per cell (Figure 4, b and c). When the length of invasive protrusions was measured from the population of cortactin-depleted *Ras^{V12}* cells still forming Lifeact puncta, we found that the average invasive protrusion length was significantly shorter compared with that in *Ras^{V12}* cells (Figure 6c). Strikingly, the distribution of invasive protrusion length became unimodal with a loss of longer invasive protrusions (Figure 6c). As we previously showed, cortactin depletion impaired the *Ras^{V12}* cells' ability to compromise the ECM and the VM (Supplemental Figure S5). Together, these results indicate that cortactin regulates both invasive protrusion formation and elongation. Furthermore, our observations suggest that the attenuation of cortactin recruitment to invasive protrusions might account for the phenotypes caused by E-cad depletion in *Ras^{V12}* cells.

DISCUSSION

In this study, we describe the unexpected role of E-cad in the invasiveness of *Ras^{V12}* cells during cell dissemination. Without E-cad, *Ras^{V12}* cells cannot invade or disseminate in vivo. E-cad/Arm subcellular distribution remodels during dissemination of *Ras^{V12}* cells, i.e., E-cad/Arm disassembles at cell–cell junctions and assembles at invasive protrusions, which are not a conventional location to detect E-cad/Arm. E-cad controls the function and elongation of invasive protrusions, not their formation. Thus loss of E-cad results in the inability of *Ras^{V12}* cells to breach the ECM and the VM. Interestingly, E-cad and cortactin influence each other's localization at invasive protrusions. Given the role of cortactin in the assembly and function of invadopodia in cancer cells, we propose that the recruitment of cortactin to invasive protrusions is the mechanism by which E-cad/Arm controls the elongation and the function of invasive protrusions. Our findings coincide with previous clinical reports describing metastasis of *E-cad+* cancers (Sundfeldt *et al.*, 1997; Kleer *et al.*, 2001; Di Venosa *et al.*, 2012; Kim *et al.*, 2016). Padmanaban *et al.* have demonstrated that E-cad promotes metastasis in multiple

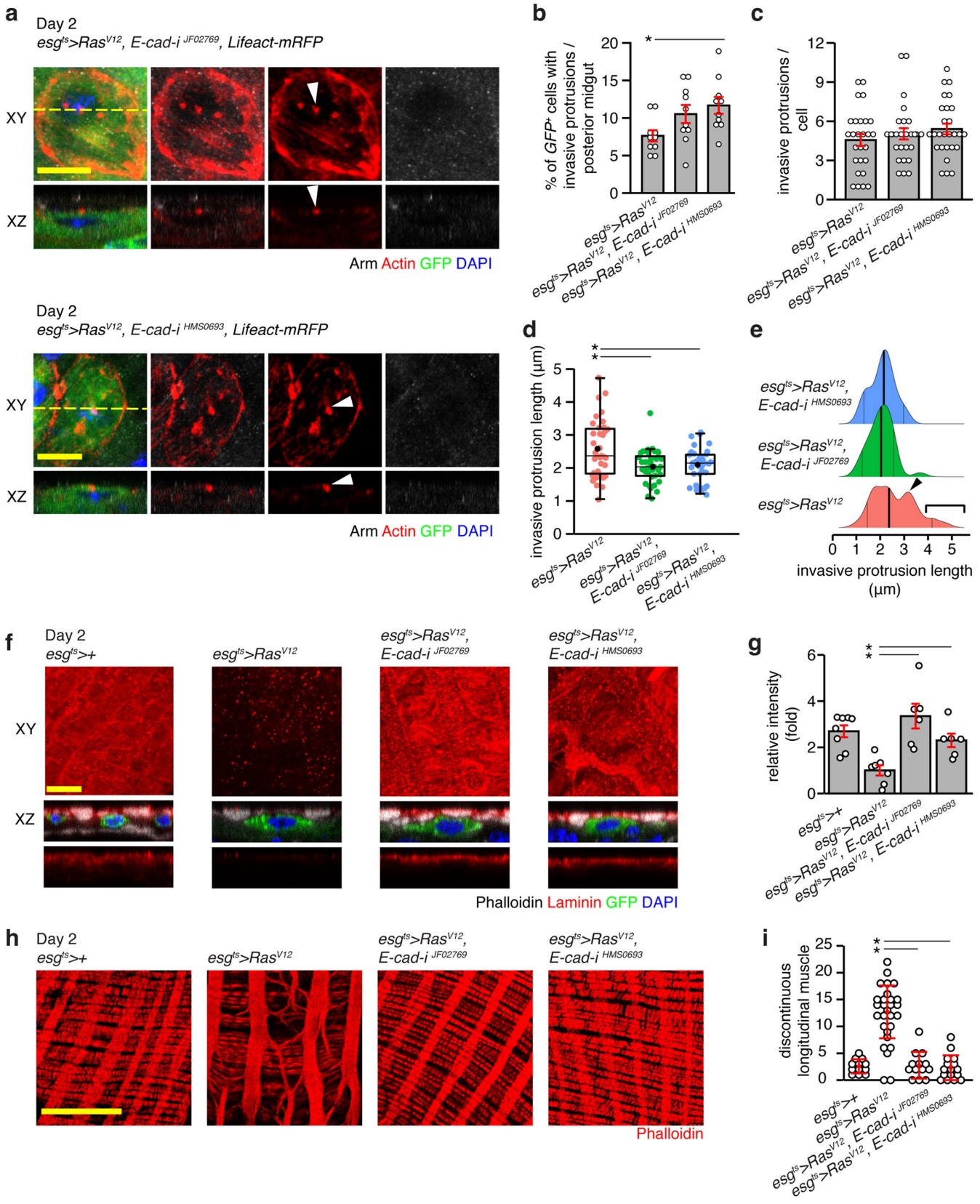

FIGURE 4: E-cad/Arm is required for the elongation and the function of invasive protrusions. (a) Lifeact-mRFP signals (red) in Ras^{V12}, *E-cad* RNAi cells (green). Nuclei are marked with DAPI. Lifeact-mRFP puncta located at the basal side of Ras^{V12} cells represent invasive protrusions (arrowheads). Two *E-cad* RNAi lines (*JF02769* and *HMS0693*) are used to knock down *E-cad* in Ras^{V12} cells. Top images (XY), basal sections; bottom images (XZ), orthogonal sections. (b) Percentage of GFP^+ cells with actin-rich invasive protrusions per midgut. $P = 0.14$ (Ras^{V12} - Ras^{V12}, *E-cad-i*^{JF02769}) and $P = 0.03$ (Ras^{V12} - Ras^{V12}, *E-cad-i*^{HMS0693}); $n = 10$ midguts. (c) Quantification of invasive protrusions per cell; $n = 24$ cells

models of breast cancer by functioning as a survival factor (Padmanaban *et al*., 2019). Our study provides new insights into how E-cad might control the initial step of metastasis.

From this study, it is unclear what E-cad binds when localized to invasive protrusions. E-cad is known to bind to N-cadherin. Thus it is possible that E-cad binds to the *Drosophila* N-cadherin ortholog Cadherin-N (CadN), which might be expressed in the VM. However, *CadN* does not appear to be expressed in the midguts based on the high-throughput sequencing data available in the FlyBase. Alternatively, E-cad might form a trans-interaction with E-cad in neighboring invasive protrusions. Considering the requirement of E-cad in invasive protrusion elongation (Figure 3), we speculate that trans-interaction between E-cads in neighboring invasive protrusions might aid the development of more prominent invasive protrusions. Further investigations might help to answer this interesting question.

Our study indicates that E-cad is a newly identified component of invasive protrusions, which are reminiscent of invadopodia observed in cancer cells. A recent preprint shows that E-cad plays a role in invadopodia formation in human cancer cells (Dobric *et al*., 2020), suggesting that the role of E-cad in cell invasion might be conserved. Given the essential role of cortactin in the assembly and function of invasive protrusions, it might be interesting to test whether E-cad also plays a role in recruiting cortactin to invadopodia.

METHODS

Drosophila stocks and husbandry

The stocks obtained from the Bloomington *Drosophila* Stock Center (BDSC), the Vienna *Drosophila* Resource Center (VDRC), and the National Institute of Genetics, Japan (NIG) are the following: *UAS-Ras^{V12}* (III) (BDSC, 4847), *UAS-E-cad-i^{JF02769}* (BDSC, 27689), *UAS-E-cad-i^{HMS0693}* (BDSC, 32904), *UAS-E-cad-GFP* (BDSC, 58445), *shg^{mTomato}* (referred as *E-cad^{mTomato}*; BDSC, 58789), *UAS-Cortactin-i^{HMS00658}* (BDRC, 32871), *UAS-Cortactin-i^{KK108594}* (VDRC, v105289), *UAS-Actin-mRFP* (BDSC, 24778), and *UAS-Lifeact-mRFP* (BDSC, 58362). We also used *UAS-Ras^{V12}* (II) (laboratory stock) and *UAS-mCherry-Moe.ABD* (FlyBase, FBtp0108918; a gift from Susan Parkhurst).

We derived transgene expression in ISCs and EBs using *esg-GAL4, tub-GAL80^{ts},* and *UAS-GFP* (*esg^{ts}*) (laboratory stock) as described previously (Kwon *et al*., 2015; Lee *et al*., 2020). Intestinal epithelial cells manipulated by *esg^{ts}* are marked by GFP. Fly crosses were raised in the standard cornmeal-agar medium at 18°C throughout development and adulthood. Three- to 10-day-old nonvirgin female flies were used for all the experiments. To induce transgenes, flies were shifted to 29°C for 1 to 2 d prior to dissection.

E-cad RNAi knockdown efficiency was assessed from the wing imaginal discs of third instar larvae via qRT-PCR. RNAi was expressed with *nub-GAL4*. RNAi line (knockdown efficiency): *UAS-E-cad-i^{JF02769}* (~67%), *UAS-E-cad-i^{HMS0693}* (~63%), *UAS-Cortactin-i^{HMS00658}* (~77%), and *UAS-Cortactin-i^{KK108594}* (~61%). Primer sequences for *E-cad*: 5′-GAATCCATGTCGGAAAATGC-3′ and 5′-GTCACTGGCGCTGATAGTCA-3′; primer sequences for *Cortactin*: 5′-GGTGGAGAAGCACGAGTCTC-3′ and 5′-ACTTGTCCTTTCGGTCCTCC-3′. For each independent experiment, 30 imaginal discs (one imaginal disc per larva) were dissected for each genotype. Three independent experiments were carried out each with three technical replicates. A total of 90 imaginal discs were used per genotype.

Immunostaining

We used the following primary antibodies: mouse anti-Arm (1:100; DSHB, N27A1), rat anti-E-cad antibody concentrate (1:50; DSHB, DCAD2), rabbit anti-Laminin (1:100; Abcam, ab47650), and mouse anti-Mmp1 (1:1000; DSHB, 3B8D12). Alexa Fluor secondary antibodies raised in goat (A11012, A11005, A21244, A21235) were obtained from Thermo Fisher Scientific and used at a dilution of 1:1000. We stained F-actin with phalloidin conjugated to Alexa 594 or 647 (1:1000, Thermo Fisher Scientific, A12381 and A22287). DAPI was used at a 1:2000 dilution (Sigma-Aldrich, D9542).

We fed flies 4% sucrose for approximately 4 h prior to dissection to remove food from the midgut. Midguts from the adult female flies were then dissected in phosphate-buffered saline (PBS), pH 7.4, and fixed for 20 min at room temperature in 4% paraformaldehyde (Electron Microscopy Sciences, RT15710) diluted in PBS. Midguts were washed three times in PBST (PBS supplemented with 0.2% Triton X-100) and then blocked overnight in PBST supplemented with 5% normal goat serum at 4°C. The tissue samples were then incubated with primary antibody in PBST supplemented with 5% normal goat serum for 2–3 h at room temperature and rinsed three times in PBST. Secondary antibodies and DAPI were diluted together in PBST supplemented with 5% normal goat serum and incubated with samples at room temperature for 1–2 h. After secondary incubation, the samples were rinsed three times in PBST and mounted in Vectashield (Vector Laboratories, H1000).

were counted from 8 midguts for each genotype. $P = 0.72$ (*Ras^{V12} - Ras^{V12}, E-cad-i^{JF02769}*) and $P = 0.35$ (*Ras^{V12} - Ras^{V12}, E-cad-i^{HMS0693}*). In b and c, mean ± SEMs are shown with individual data points, and statistical analysis was performed using one-way ANOVA with post-hoc Tukey HSD. (d) Quantification of actin-rich invasive protrusion length. Results are shown in boxplots (center line, median; black circle, mean; box, IQR; whiskers extending to ± 1.5 × IQR). $P = 0.02$ (*Ras^{V12} - Ras^{V12}, E-cad-i^{JF02769}*) and $P = 0.03$ (*Ras^{V12} - Ras^{V12}, E-cad-i^{HMS0693}*); $n = 36$ invasive protrusions from 12 cells and 6 posterior midguts. The statistical significance was assessed by Kruskal–Wallis and Dunn's test. (e) Distribution of invasive protrusion length. Lines in the histogram indicate the median (center) and the IQR (right and left). (f) Laminin B1 staining. Top images, top views (xy); bottom images, orthogonal sections (xz). *Ras^{V12}* cells are marked with GFP (green). All genotypes were stained with anti-Laminin B1 antibody (red), phalloidin (gray), and DAPI (blue). Scale bars, 10 µm. (g) Quantification of Laminin B1 signals. From left to right, $P = 8.95 \times 10^{-06}$ (*Ras^{V12} - Ras^{V12}, E-cad-i^{JF02769}*) and $P = 0.02$ (*Ras^{V12} - Ras^{V12}, E-cad-i^{HMS0693}*); $n = 8$ (*esg^{ts}*), $n = 7$ (*esg^{ts}>Ras^{V12}*), $n = 6$ (*esg^{ts}>Ras^{V12}, E-cad-i^{JF02769}*), and $n = 6$ (*esg^{ts}>Ras^{V12}, E-cad-i^{HMS0693}*) midguts. (h) VM at the posterior midguts. VM (red) is visualized with phalloidin. Scale bars, 50 µm. (i) Quantification of longitudinal muscle damage. From left to right, $P = 5.45 \times 10^{-13}$ (*Ras^{V12} - Ras^{V12}, E-cad-i^{JF02769}*) and $P = 9.24 \times 10^{-14}$ (*Ras^{V12} - Ras^{V12}, E-cad-i^{HMS0693}*); $n = 12$ (*esg^{ts}*), $n = 27$ (*esg^{ts}>Ras^{V12}*), $n = 13$ (*esg^{ts} > Ras^{V12}, E-cad-i^{JF02769}*), and $n = 16$ (*esg^{ts}>Ras^{V12}, E-cad-i^{HMS0693}*) midguts. In g and i, mean ± SEMs are shown with individual data points. Data were analyzed by using one-way ANOVA with post-hoc Tukey HSD. Asterisks indicate statistical significance ($P < 0.05$). If not noted, differences were not significant at the 0.05 level. Transgenes were expressed with *esg^{ts}*for 2 d by shifting to 29°C.

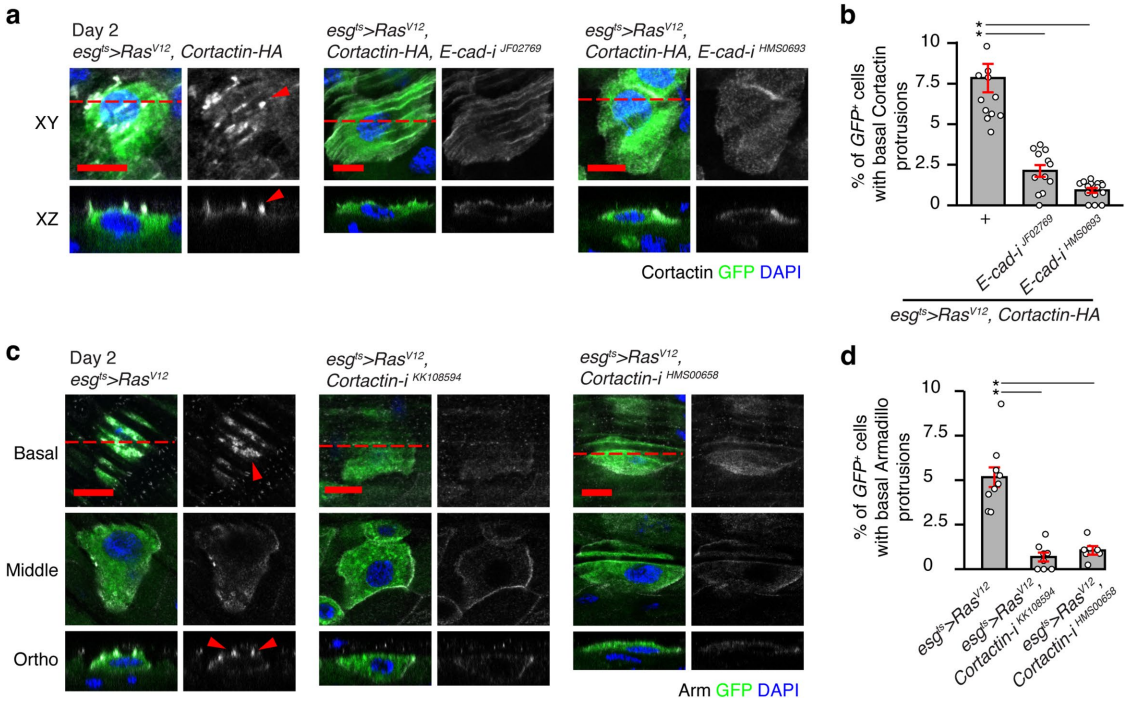

FIGURE 5: E-cad and cortactin influence each other's localization to invasive protrusions. (a) Cortactin localization. *UAS-Cortactin-HA* was combined with *esg*^{ts}. Cortactin-HA (red) in *Ras*^{V12} cells is detected with anti-HA staining, and nuclei are marked with DAPI (blue). (b) Quantification of *GFP*$^{+}$ cells with cortactin-rich invasive protrusions. $P = 4.72 \times 10^{-8}$ (*Ras*^{V12}, *Cortactin-HA* - *Ras*^{V12}, *Cortactin-HA, E-cad-i*^{JF02769}) and $P = 2.14 \times 10^{-10}$ (*Ras*^{V12}, *Cortactin-HA* - *Ras*^{V12}, *Cortactin-HA, E-cad-i*^{HMS0693}); $n = 13$ (*esg*^{ts}>*Ras*^{V12}, *Cortactin-HA*), $n = 12$ (*esg*^{ts}> *Ras*^{V12}, *Cortactin-HA, E-cad-i*^{HMS0693}), and $n = 14$ (*esg*^{ts}> *Ras*^{V12}, *Cortactin-HA, E-cad-i*^{JF02769}) midguts. (c) Arm localization in *Ras*^{V12} cells (green). Arm is detected with anti-Arm antibody (gray), and nuclei with DAPI (blue). Red arrowheads indicate Arm basal puncta. Scale bar, 10 μm. (d) Quantification of cells with Arm basal puncta. $P = 2.08 \times 10^{-10}$ (*Ras*^{V12} - *Ras*^{V12}, *Cortactin-i*^{KK108594}) and $P = 5.51 \times 10^{-11}$ (*Ras*^{V12} - *Ras*^{V12}, *Cortactin-i*^{HMS00658}); $n = 14$ (*esg*^{ts}>*Ras*^{V12}), $n = 10$ (*esg*^{ts}>*Ras*^{V12}, *Cortactin-i*^{KK108594}), and $n = 12$ (*esg*^{ts}>*Ras*^{V12}, *Cortactin-i*^{HMS00658}) midguts. For b and d, mean ± SEMs are shown with individual data points. Data were analyzed by using one-way ANOVA with post-hoc Tukey HSD. Asterisks indicate statistical significance ($P < 0.05$). If not noted, differences were not significant at the 0.05 level. For a and c, transgenes were expressed with *esg*^{ts} for 2 d.

Image acquisition and quantification

Samples were imaged using a Leica SP8 laser scanning confocal microscope with 40×/1.25 oil or 63×/1.4 oil objective lenses, and confocal stacks (0.8 μm step size or 0.25 μm for higher resolution images) were processed and analyzed using Fiji (ImageJ, National Institutes of Health).

We quantified disseminated cells by counting GFP^{+}, DAPI^{+} cells detected on the outer surface of the VM (Lee *et al.*, 2020). Confocal stacks (0.8 μm step size) of the posterior midgut were captured in 388 μm × 388 μm fluorescent images. The orthogonal view feature in Fiji was used to determine the position of disseminated cells. Graphical representations of all data points were generated as bar charts with data point overlap in R.

To quantify longitudinal muscle breakage, we visualized the VMs by staining with phalloidin (Lee *et al.*, 2020). Longitudinal muscle breakage was quantified from one leaflet of the confocal stacks (0.8 μm step size). Fluorescent images (388 μm × 388 μm) were acquired from the posterior midgut with 40×/1.25 oil objective. Graphical representations of all data points were generated as ggplot2 dot plots in R.

Mmp1 fluorescence intensity was quantified from the posterior midgut as described previously (Lee *et al.*, 2020). Laser settings were kept identical for capturing midgut images. Confocal planes covering one leaflet of the midgut along the apical-basal axis were projected to generate the 388 μm × 388 μm microscope field projection. We collected mean intensity values from three random 100 μm × 100 μm fields per midgut using Fiji and subtracted background values from the area outside surrounding the intestine. Graphical representations of all data points were generated as bar charts with data point overlap in R.

To measure fluorescent intensity of Laminin B1, we generated z-projection (388 μm × 388 μm) of confocal stacks covering one leaflet of the posterior midgut. Mean gray values from three random 100 μm × 100 μm regions per midgut were collected. The background was then subtracted using values from the area outside the intestine. Graphical representations of all data points were generated as bar charts with data point overlap in R.

We quantified cells with ARM basal invasive protrusions by counting GFP^{+}, DAPI^{+} having Arm^{+} basal protrusions by using Fijis orthogonal view function. The 63×/1.4 oil objective covering a 246.27 μm × 246.27 μm in area was used to acquire images from the R5 region of the posterior midgut. The number of cells with Arm basal protrusions was then divided by the total number of GFP^{+}, DAPI^{+} cells in the gut area imaged. Actin-rich invasive protrusions were quantified in a similar manner, however, instead of using Arm as the marker to detect invasive protrusions, we quantified actin basal protrusions by expressing *UAS-Lifeact-mRFP*. Graphs illustrating the percentage of cells with invasive protrusions per midgut were generated in R.

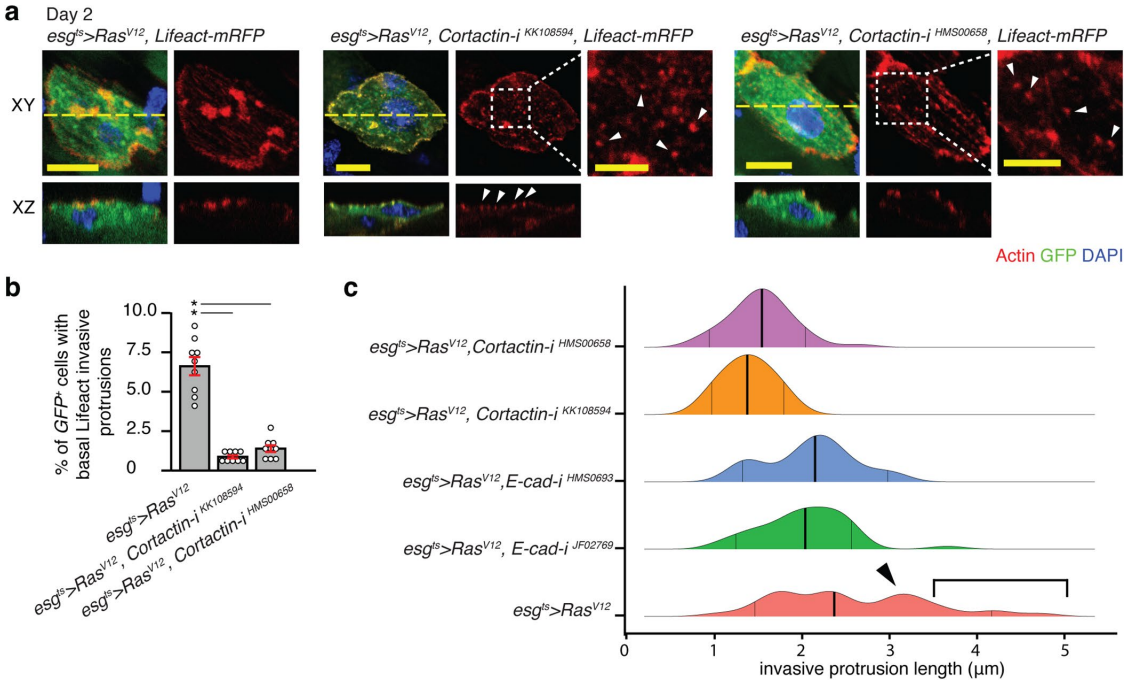

FIGURE 6: Cortactin is important for the formation and elongation of invasive protrusions. (a) Actin-rich basal puncta. Actin is visualized with Lifeact (red) and nuclei with DAPI (blue). Scale bars, 10 μm. Transgenes were expressed with esg^{ts} for 2 d. (b) Quantification of GFP^+ cells with invasive protrusions. $P = 1.25 \times 10^{-10}$ (Ras^{V12} - Ras^{V12}, $Cortactin\text{-}i^{KK108594}$) and $P = 8.53 \times 10^{-10}$ (Ras^{V12} - Ras^{V12}, $Cortactin\text{-}i^{HMS00658}$). $n = 9$ ($esg^{ts}>Ras^{V12}$), $n = 9$ ($esg^{ts}>Ras^{V12}$, $Cortactin\text{-}i^{KK108594}$), $n = 9$ ($esg^{ts}>Ras^{V12}$, $Cortactin\text{-}i^{HMS00658}$) midguts. Mean±SEMs are shown with individual data points. Data were analyzed by using one-way ANOVA with post-hoc Tukey HSD. Asterisks indicate statistical significance ($P < 0.05$). If not noted, differences were not significant at the 0.05 level. (c) Histogram of invasive protrusion length. $esg^{ts}>Ras^{V12}$, $esg^{ts}>Ras^{V12}$, $E\text{-}cad\text{-}i^{JF02769}$, and $esg^{ts}>Ras^{V12}$, $E\text{-}cad\text{-}i^{HMS0693}$ are adapted from Figure 4e. $P = 3.26 \times 10^{-4}$ (Ras^{V12} - Ras^{V12}, $Cortactin\text{-}i^{KK108594}$), $P = 3.26 \times 10^{-4}$ (Ras^{V12} - Ras^{V12}, $Cortactin\text{-}i^{HMS00658}$), $P = 6.92 \times 10^{-3}$ (Ras^{V12} - Ras^{V12}, $E\text{-}cad\text{-}i^{JF02769}$), and $P = 1.94 \times 10^{-3}$ (Ras^{V12} - Ras^{V12}, $E\text{-}cad\text{-}i^{HMS0693}$). We performed a Fisher exact pairwise comparison for a 5×2 contingency table, invasive protrusions were categorized based on length equal to or greater than 3 μm. The p values are corrected using the FDR method for multiple hypothesis testing at a 5% cut-off; $n = 36$ invasive protrusions from 12 cells in 6 midguts.

To assess junction integrity, we measured Arm signal intensity from 10 cells per midgut. Arm signal intensity was measured using the plot profile feature in Fiji from a representative cross-section for a given cell. We measured Arm signal intently along a line drawn from the cell boundary to the nuclear boundary. We took the measured value at the midpoint of the line as the cytosolic Arm signal intensity and compared with the value obtained at the cell boundary/junction. Junction intensity of proteins in samples without obvious junctional staining was measured by using GFP to determine cell boundaries. We determined the location where the GFP signal started and measure the intensity of Arm at that location. For statistical analysis, one-way ANOVA with post-hoc Tukey HSD was performed using R.

To measure the colocalization between Arm and actin-rich at invasive protrusions, images were imported into Fiji. We created a z-stack containing an isolated area in a cell containing invasive protrusions. Then we used the plugging called JACoP, which calculates a variety of colocalization parameters, such as Pearson's coefficient and Manders' correlation. Analysis of variances (ANOVA) with post-hoc Tukey HSD (honestly significant difference) was performed using R.

We measured invasive protrusion length by using Fijis orthogonal view function. The 63×/1.4 oil objective covering 246.27 μm × 246.27 μm was used to acquire images from the R5 region of the posterior midgut. The lengths of invasive protrusions of GFP^+ cells were measured with the line tool in Fiji. We measured from the apical base of Lifeact-mRFP signals to the basal end. ANOVA with post-hoc Tukey HSD was performed using R.

Statistics and reproducibility

Statistical differences between groups of data were analyzed using a series of two-tailed unpaired Student t test, one-way ANOVA with post-hoc Tukey HSD, Fisher's exact pairwise comparisons with FDR corrected p values, or the nonparametric Kruskal–Wallis and Dunn's test with FDR correction. All statistical analyses and data graphics were done in "R" software (version 1.3.1093). All quantified experiments represent at least three biologically independent samples. Levels of significance are depicted by asterisks in the figures: $*P < 0.05$. P values are indicated in the figure legends. Sample sizes were chosen empirically based on the observed effects and listed in the figure legends. All quantifications are from the posterior midguts of the adult female flies.

DATA AVAILABILITY STATEMENT

The data supporting the finding of this study are available within the paper and as supplemental information.

ACKNOWLEDGMENTS

We thank Susan Parkhurst for sharing fly stocks, Jiae Lee for helping with imaging, and Eric So for technical assistance. This work is supported by NIH R35GM128752 to Y.V.K. and by NIH T32CA080416 to A.J.H.C.

REFERENCES

Belin BJ, Goins LM, Mullins RD (2014). Comparative analysis of tools for live cell imaging of actin network architecture. Bioarchitecture 4, 189–202.

Berx G, Cleton-Jansen AM, Nollet F, de Leeuw WJ, van de Vijver M, Cornelisse C, van Roy F (1995). E-cadherin is a tumour/invasion suppressor gene mutated in human lobular breast cancers. EMBO J 14, 6107–6115.

Berx G, Van Roy F (2001). The E-cadherin/catenin complex: an important gatekeeper in breast cancer tumorigenesis and malignant progression. Breast Cancer Res 3, 289–293.

Bogenrieder T, Herlyn M (2003). Axis of evil: molecular mechanisms of cancer metastasis. Oncogene 22, 6524–6536.

Burdsal CA, Damsky CH, Pedersen RA (1993). The role of E-cadherin and integrins in mesoderm differentiation and migration at the mammalian primitive streak. Development 118, 829–844.

Cano A, Perez-Moreno MA, Rodrigo I, Locascio A, Blanco MJ, del Barrio MG, Portillo F, Nieto MA (2000). The transcription factor snail controls epithelial-mesenchymal transitions by repressing E-cadherin expression. Nat Cell Biol 2, 76–83.

Christofori G, Semb H (1999). The role of the cell-adhesion molecule E-cadherin as a tumour-suppressor gene. Trends Biochem Sci 24, 73–76.

Clark ES, Whigham AS, Yarbrough WG, Weaver AM (2007). Cortactin is an essential regulator of matrix metalloproteinase secretion and extracellular matrix degradation in invadopodia. Cancer Res 67, 4227–4235.

Di Venosa G, Rodriguez L, Mamone L, Gandara L, Rossetti MV, Batlle A, Casas A (2012). Changes in actin and E-cadherin expression induced by 5-aminolevulinic acid photodynamic therapy in normal and Ras-transfected human mammary cell lines. J Photochem Photobiol B 106, 47–52.

Dobric A, Germain S, Bonier R, Silvy F, Audebert S, Camoin L, Dusetti N, Soubeyran P, Iovanna J, Rigot V, André F (2020). E-cadherin: Unexpected actor of invadopodia formation in pancreatic cancer. *bioRxiv*: 2020.2010.2009.332783.

Eddy RJ, Weidmann MD, Sharma VP, Condeelis JS (2017). Tumor cell invadopodia: invasive protrusions that orchestrate metastasis. Trends Cell Biol 27, 595–607.

Frixen UH, Behrens J, Sachs M, Eberle G, Voss B, Warda A, Lochner D, Birchmeier W (1991). E-cadherin-mediated cell-cell adhesion prevents invasiveness of human carcinoma cells. J Cell Biol 113, 173–185.

Gumbiner BM (2005). Regulation of cadherin-mediated adhesion in morphogenesis. Nat Rev Mol Cell Biol 6, 622–634.

Hajra KM, Chen DY, Fearon ER (2002). The SLUG zinc-finger protein represses E-cadherin in breast cancer. Cancer Res 62, 1613–1618.

Harris TJ, Tepass U (2010). Adherens junctions: from molecules to morphogenesis. Nat Rev Mol Cell Biol 11, 502–514.

Helwani FM, Kovacs EM, Paterson AD, Verma S, Ali RG, Fanning AS, Weed SA, Yap AS (2004). Cortactin is necessary for E-cadherin-mediated contact formation and actin reorganization. J Cell Biol 164, 899–910.

Herzig M, Savarese F, Novatchkova M, Semb H, Christofori G (2007). Tumor progression induced by the loss of E-cadherin independent of beta-catenin/Tcf-mediated Wnt signaling. Oncogene 26, 2290–2298.

Jeannot P, Besson A (2020). Cortactin function in invadopodia. Small GTPases 11, 256–270.

Kim SA, Inamura K, Yamauchi M, Nishihara R, Mima K, Sukawa Y, Li T, Yasunari M, Morikawa T, Fitzgerald KC, *et al* (2016). Loss of CDH1 (E-cadherin) expression is associated with infiltrative tumour growth and lymph node metastasis. Br J Cancer 114, 199–206.

Kleer CG, van Golen KL, Braun T, Merajver SD (2001). Persistent E-cadherin expression in inflammatory breast cancer. Mod Pathol 14, 458–464.

Kwon Y, Song W, Droujinine IA, Hu Y, Asara JM, Perrimon N (2015). Systemic organ wasting induced by localized expression of the secreted insulin/IGF antagonist ImpL2. Dev Cell 33, 36–46.

Larue L, Ohsugi M, Hirchenhain J, Kemler R (1994). E-cadherin null mutant embryos fail to form a trophectoderm epithelium. Proc Natl Acad Sci USA 91, 8263–8267.

Lee J, Cabrera AJH, Nguyen CMT, Kwon YV (2020). Dissemination of Ras(V12)-transformed cells requires the mechanosensitive channel Piezo. Nat Commun 11, 3568.

Liu R, Woolner S, Johndrow JE, Metzger D, Flores A, Parkhurst SM (2008). Sisyphus, the Drosophila myosin XV homolog, traffics within filopodia transporting key sensory and adhesion cargos. Development 135, 53–63.

Lohmer LL, Kelley LC, Hagedorn EJ, Sherwood DR (2014). Invadopodia and basement membrane invasion in vivo. Cell Adh Migr 8, 246–255.

Magalhaes MA, Larson DR, Mader CC, Bravo-Cordero JJ, Gil-Henn H, Oser M, Chen X, Koleske AJ, Condeelis J (2011). Cortactin phosphorylation regulates cell invasion through a pH-dependent pathway. J Cell Biol 195, 903–920.

Mendonsa AM, Na TY, Gumbiner BM (2018). E-cadherin in contact inhibition and cancer. Oncogene 37, 4769–4780.

Millard TH, Martin P (2008). Dynamic analysis of filopodial interactions during the zippering phase of Drosophila dorsal closure. Development 135, 621–626.

Na TY, Schecterson L, Mendonsa AM, Gumbiner BM (2020). The functional activity of E-cadherin controls tumor cell metastasis at multiple steps. Proc Natl Acad Sci USA 117, 5931–5937.

Onder TT, Gupta PB, Mani SA, Yang J, Lander ES, Weinberg RA (2008). Loss of E-cadherin promotes metastasis via multiple downstream transcriptional pathways. Cancer Res 68, 3645–3654.

Padmanaban V, Krol I, Suhail Y, Szczerba BM, Aceto N, Bader JS, Ewald AJ (2019). E-cadherin is required for metastasis in multiple models of breast cancer. Nature 573, 439–444.

Parekh A, Weaver AM (2016). Regulation of invadopodia by mechanical signaling. Exp Cell Res 343, 89–95.

Perl AK, Wilgenbus P, Dahl U, Semb H, Christofori G (1998). A causal role for E-cadherin in the transition from adenoma to carcinoma. Nature 392, 190–193.

Petrova YI, Schecterson L, Gumbiner BM (2016). Roles for E-cadherin cell surface regulation in cancer. Mol Biol Cell 27, 3233–3244.

Ren G, Helwani FM, Verma S, McLachlan RW, Weed SA, Yap AS (2009). Cortactin is a functional target of E-cadherin-activated Src family kinases in MCF7 epithelial monolayers. J Biol Chem 284, 18913–18922.

Riedl J, Crevenna AH, Kessenbrock K, Yu JH, Neukirchen D, Bista M, Bradke F, Jenne D, Holak TA, Werb Z, *et al* (2008). Lifeact: a versatile marker to visualize F-actin. Nat Methods 5, 605–607.

Semb H, Christofori G (1998). The tumor-suppressor function of E-cadherin. Am J Hum Genet 63, 1588–1593.

Spracklen AJ, Fagan TN, Lovander KE, Tootle TL (2014). The pros and cons of common actin labeling tools for visualizing actin dynamics during Drosophila oogenesis. Dev Biol 393, 209–226.

Strobl-Mazzulla PH, Bronner ME (2012). Epithelial to mesenchymal transition: new and old insights from the classical neural crest model. Semin Cancer Biol 22, 411–416.

Sundfeldt K, Piontkewitz Y, Ivarsson K, Nilsson O, Hellberg P, Brannstrom M, Janson PO, Enerback S, Hedin L (1997). E-cadherin expression in human epithelial ovarian cancer and normal ovary. Int J Cancer 74, 275–280.

Thiery JP, Acloque H, Huang RY, Nieto MA (2009). Epithelial-mesenchymal transitions in development and disease. Cell 139, 871–890.

Uruno T, Liu J, Zhang P, Fan Y, Egile C, Li R, Mueller SC, Zhan X (2001). Activation of Arp2/3 complex-mediated actin polymerization by cortactin. Nat Cell Biol 3, 259–266.

Vleminckx K, Vakaet L Jr., Mareel M, Fiers W, van Roy F (1991). Genetic manipulation of E-cadherin expression by epithelial tumor cells reveals an invasion suppressor role. Cell 66, 107–119.

Weaver AM, Karginov AV, Kinley AW, Weed SA, Li Y, Parsons JT, Cooper JA (2001). Cortactin promotes and stabilizes Arp2/3-induced actin filament network formation. Curr Biol 11, 370–374.